Journal of Computational and Applied Mathematics 235 (2011) 4780–4795

Contents lists available at ScienceDirect

Journal of Computational and Applied Mathematics

journal homepage: www.elsevier.com/locate/cam

Streamwise oscillations of a cylinder beneath a free surface: Free surface effects on vortex formation modes

Canan Bozkaya [a], Serpil Kocabiyik [a,*], L.A. Mironova [a], O.I. Gubanov [b]

[a] Department of Mathematics and Statistics, Memorial University of Newfoundland, St. John's, NL, A1C 5S7, Canada

[b] Department of Mechanical Engineering, McGill University, Montreal, QC, H3A 2K6, Canada

ARTICLE INFO

Article history:
Received 1 February 2010
Received in revised form 27 August 2010

Keywords:
Two-phase viscous incompressible flow
Forced streamwise oscillation
Volume-of-fluid method
Finite volume method

ABSTRACT

A computational study of a viscous incompressible two-fluid model with an oscillating cylinder is investigated at a Reynolds number of 200 and at a dimensionless displacement amplitude of $A = 0.13$ and for the dimensionless forcing cylinder oscillation frequency-to-natural vortex shedding frequency ratios, $f/f_0 = 1.5, 2.5, 3.5$. Specifically, two-dimensional flow past a circular cylinder subject to forced in-line oscillations beneath a free surface is considered. The method is based on a finite volume discretization of the two-dimensional continuity and unsteady Navier–Stokes equations (when a solid body is present) on a fixed Cartesian grid. Two-fluid model based on improved volume-of-fluid method is used to discretize the free surface interface. The study focuses on the laminar asymmetric flow structure in the near wake region and lock-on phenomena at a Froude number of 0.2 and for the dimensionless cylinder submergence depths, $h = 0.25, 0.5$ and 0.75. The equivorticity patterns and pressure distribution contours are used for the numerical flow visualization. The code validations in special cases show good comparisons with previous numerical results.

1. Introduction

The interaction of a free surface wave motion with moving cylindrical bodies has been principally the subject of experimental studies (see e.g., [1–3]). Computations of nonlinear viscous free surface problems including cylindrical bodies are relatively few (see e.g., [4,5]). The purpose of this paper is to numerically investigate a viscous incompressible fluid flow past a circular cylinder beneath the free surface based on a two-fluid model. The aggregated-fluid approach is used by describing the behaviour of both fluids using one set of governing equations, namely the two-dimensional continuity and unsteady Navier–Stokes equations in their pressure–velocity formulation (when a solid body is present). The method of solution is based on a finite volume discretization of the governing equations. A second-order accurate central-difference scheme is used to discretize the governing equations in space in conjunction with the first-order explicit forward Euler scheme to advance these equations in time.

In the present two-fluid model, the free surface interface is discretized with the volume-of-fluid method due to Hirt and Nichols [6]. To capture the free surface, the known fluid interface geometry is used to compute fluid volume fraction, F, between zero and one in each computational cell, whose value is one for full cells; zero for cells without fluid; between zero and one for partially filled cells. At any time in the solution, the shape of the free surface interface is reconstructed using the piecewise linear interface calculation algorithm following the works in [7,8]. Since the free surface interface is free to move, its advection in time should be performed after the new velocity field has been calculated from the governing equations. In

* Corresponding author.
E-mail address: serpil@mun.ca (S. Kocabiyik).

0377-0427/$ – see front matter © 2010 Elsevier B.V. All rights reserved.
doi:10.1016/j.cam.2010.09.018

the present numerical algorithm, the strictly mass conserving volume-of-fluid advection method, for incompressible flows on a Cartesian mesh, due to Aulisa et al. [9] is used unlike the volume-of-fluid advection algorithms by [10,11] in which the advection operations may result in undershoots or overshoots of the volume fraction, and thus they do not preserve mass exactly.

For the moving fluid–body interface the fractional area/volume obstacle representation method due to Hirt and Sicilian [12] is combined with the cut cell method due to Gerrits [7] in order to improve the accuracy of the fluid–body interface approximation and preserve a global second-order accuracy of the spatial discretization. It is noted that the fractional area/volume obstacle representation method approximates fluid–body interface with straight-line segments within each computational cell using the piecewise linear interface computation algorithm and hence this method is of only first-order accurate. This complicates the numerical approximation of convective and diffusive fluxes near fluid–body interface as well as the application of the boundary conditions at fluid–body interface. In the present model, Gerrits' cell merging procedure is utilized in which the velocity cells cut by the fluid–body interface are merged with the appropriate neighbour fluid cells to form trapezoidal cells near the surface of the cylinder. A combination of *B*-spline and polynomial interpolations is then used to evaluate convective and diffusive fluxes through the edges of the trapezoidal cells. Discrete pressure and velocity fields corresponding to the successive time instants are obtained as a result of solution of a coupled sparse linear system in primitive variables using a generalized minimal residual method. This is done by making use of the Trilinos numerical solver library (see [13] for details). A preconditioner is calculated at each iteration to achieve optimal convergence for the system. The accuracy checks indicate that the present method is of second-order in space and first-order in time.

The objective of this study is to numerically investigate two-dimensional flow past a circular cylinder subject to forced streamwise oscillations beneath a free surface based on a two-fluid model at a Reynolds number of 200 and at a dimensionless displacement amplitude of $A = 0.13$ and for the dimensionless forcing cylinder oscillation frequency-to-natural vortex shedding frequency ratios, $f/f_0 = 1.5, 2.5, 3.5$. To date analysis of locked-on flow regimes in the near wake region at a Froude number of $\mathrm{Fr} = 0.2$, the dimensionless cylinder submergence depths $h = 0.25$, 0.5 and 0.75 have not been available. This study focuses on this analysis based on the numerical flow visualization in terms of the equivorticity patterns and pressure distribution contours. The observed features are compared with the case when the free surface is absent ($h = \infty$) to better understand the effect from the inclusion of the free surface. The numerical algorithm is verified by applying it to special cases in the absence of a free surface. The validation of the method is also presented for uniform flow past a stationary cylinder in the presence of a free surface. Comparisons are made with previous numerical results.

2. Model description

A basic schematic that illustrates the problem is shown in Fig. 1, together with important dimensions. In this figure, the cylinder of radius d is submerged in the fluid at the distance h^* below undisturbed free surface, g^* is the acceleration due to gravity, $\vec{g}^* = (0, g^*, 0)$, f^* is the frequency of the forced cylinder oscillation. The flow is from left to right which involves the two-fluid phases (the fluids in the regions Ω_1 and Ω_2) entering into the domain with the same uniform stream velocity, U. The fluids in Ω_1 and Ω_2 have the densities, ρ_1, ρ_2, and the dynamic viscosities, μ_1, μ_2, respectively. The cylinder is initially at rest in a uniform flow with velocity U, and then, at time $t^* = 0$, the cylinder starts to perform time-dependent streamwise oscillation. The imposed dimensionless oscillatory cylinder displacement is assigned by $x(t) = A\cos(2\pi ft)$. The dimensionless parameters are the forcing amplitude of the cylinder oscillations, $A = A^*/d$; the frequency ratio, f/f_0, with $f = df^*/U$ and $f_0 = df_0^*/U$ being the dimensionless forcing frequency of the cylinder oscillation and the natural vortex shedding frequency; the Froude number, $\mathrm{Fr} = U/\sqrt{dg^*}$, and the dimensionless cylinder submergence depth, $h = h^*/d$. Here, f_0^* is the dimensional natural vortex shedding frequency of a stationary cylinder and $t = t^*U/d$ is the dimensionless time. The Reynolds number is defined by $R = Ud/\nu_1$ and $R = Ud/\nu_2$ for fluids with the kinematic viscosities $\nu_1 = \mu_1/\rho_1$ and $\nu_2 = \mu_2/\rho_2$ in Ω_1 and Ω_2, respectively. The dimensionless period of cylinder oscillation, $T(=1/f)$, is $T = T^*U/d$. Different investigators used various combinations of relevant periodic motion parameters, A or a period parameter, V_mT/d, (Keulegan–Carpenter number, KC, where V_m is the maximum oscillatory velocity), and the forcing frequency parameter f. If the parameters of the present problem characterizing the periodic motion, are introduced, as defined above, then $A = KC/2\pi$.

2.1. Governing equations

The present two-fluid flow model involves modelling of both fluids in flow domains Ω_1 and Ω_2 using the same single-fluid flow model equations employed in [14]. In Gubanov's work generalized differentiation is utilized to extend the Reynolds transport theorem over a control volume containing fluid interface for deriving the integral form of governing equations for the incompressible viscous flow problems involving arbitrarily moving bodies. This is done by following the work in [15], and the use of generalized function theory made this derivation straightforward, systematic and rigorous (see [14,5], for more details). The continuity and Navier–Stokes equations proposed in [14] (when a solid body is present) are summarized in a non-inertial frame of reference which translates with the cylinder as follows

$$\frac{\mathrm{d}\mathbb{V}}{\mathrm{d}t} + \int_{\mathbb{A}} (\vec{u}\cdot\vec{n})\,\mathrm{d}S = 0, \tag{1}$$

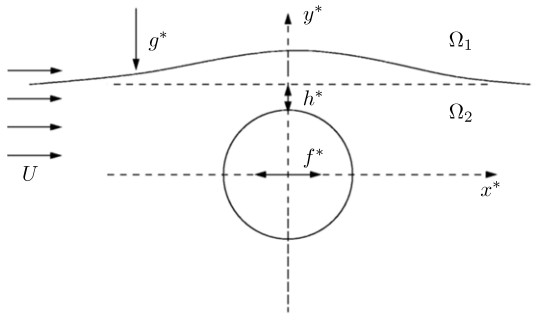

Fig. 1. Schematic of the problem.

$$\frac{\mathrm{d}}{\mathrm{d}t}\int_{\mathbb{V}} u\,\mathrm{d}V + \int_{\mathbb{A}} (\vec{n}\cdot\vec{u})u\,\mathrm{d}S = -\frac{1}{\varepsilon}\int_{\mathbb{A}\mathbb{U}\mathbb{I}} pn_1\,\mathrm{d}S + \frac{1}{R}\int_{\mathbb{A}\mathbb{U}\mathbb{I}} \vec{n}\cdot\nabla u\,\mathrm{d}S - \int_{\mathbb{V}} a_1\,\mathrm{d}V, \tag{2}$$

$$\frac{\mathrm{d}}{\mathrm{d}t}\int_{\mathbb{V}} v\,\mathrm{d}V + \int_{\mathbb{A}} (\vec{n}\cdot\vec{u})v\,\mathrm{d}S = -\frac{1}{\varepsilon}\int_{\mathbb{A}\mathbb{U}\mathbb{I}} pn_2\,\mathrm{d}S + \frac{1}{R}\int_{\mathbb{A}\mathbb{U}\mathbb{I}} \vec{n}\cdot\nabla v\,\mathrm{d}S + \int_{\mathbb{V}} \left(\frac{1}{\mathrm{Fr}^2} - a_2\right)\mathrm{d}V, \tag{3}$$

where $\mathbb{V}$ and $\mathbb{A}$ are the fractional volume and area, respectively, open to flow within the computational cell, V; $\mathbb{I}$ is the length of the fluid–body interface open to flow; $\vec{u}$ is the dimensionless velocity vector, where $\vec{u} = (u, v, 0)$; $\vec{n}$ is the outward unit normal vector; S is the control volume boundary. All quantities in governing equations (1)–(3) are given in their dimensionless form. These quantities are defined in terms of the dimensional counterparts: $x = x^*/d, y = y^*/d, u = u^*/U, v = v^*/U, V = V^*/d^2, S = S^*/d, \mathbb{V} = \mathbb{V}^*/d^2, \mathbb{A} = \mathbb{A}^*/d, \mathbb{I} = \mathbb{I}^*/d$. The dimensionless pressure is given by $p/\varepsilon = p^*/\rho_2 U^2$, where $\varepsilon = \rho_1/\rho_2$ when $\vec{x} \in \Omega_1$, and $\varepsilon = 1$ when $\vec{x} \in \Omega_2$. The external force, $\vec{F}$, is due to the dimensionless acceleration of the non-inertial frame of reference, $\vec{a} = (a_1^* d/U^2, a_2^* d/U^2, 0)$, and due to the dimensionless gravity force, $\vec{g} = (0, 1/\mathrm{Fr}^2, 0)$, which yields $\vec{F} = (-a_1, 1/\mathrm{Fr}^2 - a_2, 0)$.

Numerical experiments conducted in the present study show that when the cylinder moves through the fixed staggered grid, the pressure cell which belongs to the cylinder at time $t = t^n$ may become the fluid cell at time $t = t^{n+1}$. The continuity equation needs to be discretized in this pressure cell. Since at time $t = t^n$ the velocities in the pressure cell do not satisfy the mass balance exactly, the pressure field has to do extra work to restore the mass balance in the pressure cell at time $t = t^{n+1}$. This extra work seems to reflect as a spike in the pressure. Fekken [16] and Kleefsman [17] attempted to overcome this difficulty but they failed to eliminate these pressure spikes. In the present computational model, the pressure spikes are eliminated by using the non-inertial frame of reference which translates with the cylinder. The single set of governing equations (1)–(3) are solved in the flow part of the computational domain, $\Omega = \Omega_1 \cup \Omega_2$, shown in Fig. 1, after setting the fluid properties, $\rho_1/\rho_2 = 1/100$ and $\mu_1/\mu_2 = 1/100$ (or $\nu_1/\nu_2 = 1$), following the work of Reichl et al. [4]. Therefore, the Reynolds numbers in the fluid regions Ω_1 and Ω_2 are the same which is varied by altering the viscosity. In Gubanov's [14] work, the motion of the fluid in Ω_1 is neglected and the effect of the ambient pressure exerted on the fluid in Ω_1 by the fluid in Ω_2 is taken into consideration. Thus, the governing equations are solved in the region Ω_2 only. Consequently, the free surface is modelled explicitly at the computational boundary. This results in numerical difficulties due to the complexity of application of boundary conditions at the free surface on the non-boundary-fitted Cartesian grid.

3. Numerical method

Following the work in [5], the continuity and Navier–Stokes equations are discretized using a finite volume approximation for two fluid regions Ω_1 and Ω_2 on a fixed Cartesian grid. This is done based on the aggregated-fluid approach by describing the behaviour of both fluids using one set of Eqs. (1)–(3). In this approach the free surface is no longer the boundary of the calculation domain but just the interface between two fluids. This prevents difficulties with free surface conditions reported in [14] but imposes new challenges as a discontinuity is introduced in the fluid properties across the interface. A second-order accurate central-difference scheme is used to discretize the governing equations in space in conjunction with first-order explicit forward Euler scheme to advance the numerical solution in time. A cell merging procedure is used to preserve a global second-order accuracy of the spatial discretization. The no-slip boundary conditions are implemented on the surface of the cylinder. At the inflow boundary of the computational domain, the uniform free stream conditions are prescribed. Well-posed open boundary conditions, due to Gresho and Sani [18],

$$\frac{1}{R}\frac{\partial u}{\partial x} + \frac{\bar{h}}{\mathrm{Fr}^2} = p, \qquad \frac{\partial v}{\partial x} = 0 \tag{4}$$

are enforced at the outflow boundary. Here $\bar{h}$ is the height of the fluid at the outflow boundary. At the top and bottom boundaries of the computational domain, the free-slip boundary conditions are prescribed. The uniform flow is used as the

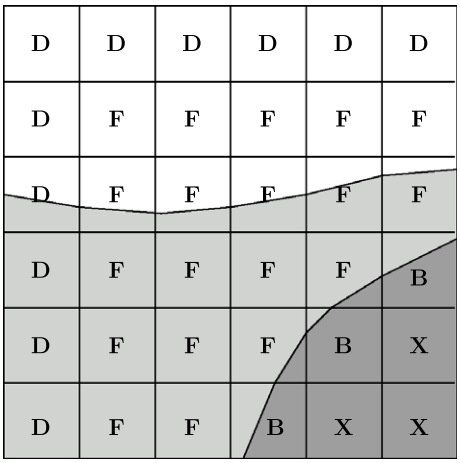

Fig. 2. An example of pressure cell labeling.

initial condition. It is assumed that at time $t = 0$, the free surface is undisturbed. The present paper adopts basically the same numerical method of solution as that used in [5], and a summary of the numerical method is given below.

3.1. Cell labeling

The governing equations and the boundary conditions are discretized on a staggered grid. The cell labeling is used to identify cells of different types. This is done by following the work of Gerrits and Veldman [19]. For pressure cells four different cell types are distinguished. Cells for which the fluid in Ω_1 and the fluid in Ω_2 occupy more than a half cell are marked as **F**(luid). **B**(oundary) cells are the ones located in a vicinity of fluid–body interface. Cells located at the computational domain boundary are labeled as **D**(omain). Cells occupied by the body are called (e)**X**(cluded). The continuity equation is discretized in all **F** cells. The value of pressure is set to zero in **B**, **D** and **X** knots. An example of pressure cells labeling is shown in Fig. 2. Next, velocity cells are labeled in the following manner: the edge of pressure cell on which u- or v-velocity knot is located is labeled according to the types of pressure cells this edge belongs to. For example, the edge between two **F** cells is denoted as **FF** edge. As a result, seven types of velocity cells can be distinguished: **FF**, **BF**, **BX**, **DF**, **BB**, **DD** and **XX**. The Navier–Stokes are discretized in all **FF** cells. The values of velocities **BF**, **BB**, **BX** and **XX** are set to zeros. **DF** and **DD** velocities are used to apply boundary conditions at the computation domain boundary.

3.2. Discretization of the continuity equation

Fig. 3 shows a pressure cell, $p_{i,j}$, which is cut by the presence of a fluid–body interface. When solving the continuity equation (1) in this cell, the finite volume discretization yields

$$-(u_{i,j}\mathbb{A}_0)^{n+1} + (u_{i+1,j}\mathbb{A}_1)^{n+1} - (v_{i,j}\mathbb{A}_2)^{n+1} + (v_{i,j+1}\mathbb{A}_3)^{n+1} = 0, \tag{5}$$

where $\mathbb{A}_k$, $k = 0 \ldots 3$ indicate the areas open to flow in the $p_{i,j}$ cell as shown in Fig. 3.

3.3. Discretization of the Navier–Stokes equations

The momentum equations (2) and (3) are solved in u- and v-cells, respectively. In what follows, only the discretization of the u-momentum equation (2) is discussed; the discretization of the v-momentum equation (3) follows a similar approach. If **FF** cell is not in a vicinity of the fluid–body interface, its neighbour velocity cells will be one of the following types: **FF**, **DF** or **DD**. In this situation, a standard discretization is used to discretize the Navier–Stokes equations [20]. However, when **FF** cell borders at least one cell of **BF** type (i.e., **FF** knot is in a vicinity of the fluid–body interface), a standard discretization of the u-momentum equation (2) will result in the loss of accuracy. The typical situation when **FF** cell (ABCDEG) borders **BF** cell (GEF) is shown in Fig. 4. Many studies exclude **BF** cells from consideration and apply a no-slip condition to calculate **BF**-velocity (see, for example, [14,17,16,7]). Gubanov [14] pointed out that the loss of accuracy in the vicinity of the fluid–body interface due to excluding **BF** cells greatly affects hydrodynamic forces imposed on this interface. In the present model, a cell merging technique is used to discretize the Navier–Stokes equations in such **FF** cells to ensure that the second-order accuracy is preserved. For example, in Fig. 4, **FF** cell (ABCDEG) can be merged with the **BF** cell (GEF) to form a trapezoidal cell near the surface of the cylinder. Depending on the location and the local orientation of the fluid–body interface, cells of a wide variety of shapes can be formed. An approximation to the velocity knots for which a standard discretization is not

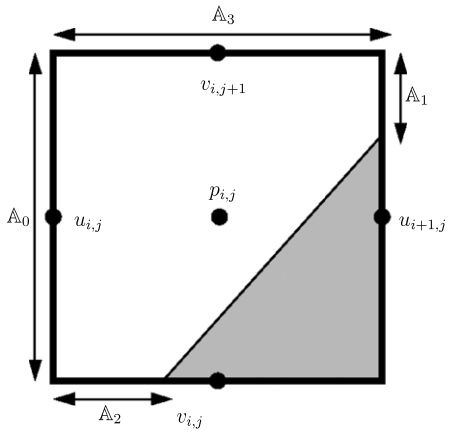

Fig. 3. Discretization of the continuity equation (1). The part of the cell occupied by the cylinder is shown in gray.

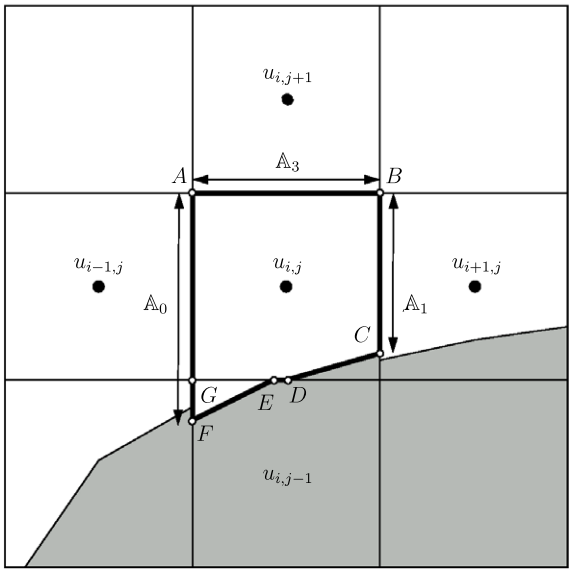

Fig. 4. Discretization of the u-momentum equation (2). **FF** cell (ABCDEG) borders **BF** cell (GEF).

applicable is then obtained by using a two-dimensional spline interpolating function implemented in SINTEF multilevel B-spline approximation library (available at www.sintef.no). The B-spline interpolation allows a second-order approximation of the velocity and convective flux from available neighbouring values of the fluid velocities and the values computed from the no-slip boundary condition. An example of u-cell in which u-momentum equation (2) is discretized is shown in Fig. 4.

The time derivative is approximated in space by using the midpoint rule and in time by using the explicit forward Euler method as

$$\frac{\mathrm{d}(u_{i,j}\mathbb{V}_{u_{i,j}})}{\mathrm{d}t} \approx \frac{u_{i,j}^{n+1}\mathbb{V}_{u_{i,j}}^{n+1} - u_{i,j}^{n}\mathbb{V}_{u_{i,j}}^{n}}{\Delta t}, \tag{6}$$

where $\mathbb{V}_{u_{i,j}} = \mathbb{V}_{ABCDEG} + \mathbb{V}_{GEF}$. The convective term is discretized by

$$\int_{\mathbb{A}} (\vec{n}\cdot\vec{u})u \,\mathrm{d}S \approx \sum_{k=0}^{N'} u_{\mathbb{A}_k}^{n+1} f_{\mathbb{A}_k}^{n}, \quad N' = 2\ldots 8, \tag{7}$$

where $f_{\mathbb{A}_k}^{n}$ is the convective flux through an edge $\mathbb{A}_k$ at the time $t = t^n$, N' denotes a number of edges of u-cell for which a velocity and convective flux are evaluated. A finite volume approximation of the diffusive term for the edges of a cell $u_{i,j}$ is written as

$$\frac{1}{R}\int_{\mathbb{A}} \vec{n}\cdot\nabla u \mathrm{d}S \approx \frac{1}{R}\sum_{k=0}^{N'} \bar{f}_{\mathbb{A}_k}^{n+1} + \frac{1}{R}\sum_{k=0}^{N'} \bar{f}_{\mathbb{I}_k}^{n+1}, \quad N' = 0\ldots 8. \tag{8}$$

Here, $\bar{f}^{n+1}_{\mathbb{A}_k}$ and $\bar{f}^{n+1}_{\mathbb{I}_k}$ indicate the diffusive flux through $\mathbb{A}_k$ and $\mathbb{I}_k$, respectively, at the time $t = t^{n+1}$. It is noted that the no-slip condition is used when approximating $\bar{f}^{n+1}_{\mathbb{I}_k}$.

For the approximation of the pressure and volumetric force no merging procedure is needed since **BF** cells are excluded from the consideration. The pressure term is discretized as a boundary integral resulting in

$$\frac{1}{\varepsilon}\int_{\mathbb{I}} pn_1 \mathrm{d}S. \approx \frac{1}{\varepsilon^{n+1}}(p^{n+1}_{i,j} n_{\mathbb{I}_0} \mathbb{I}^{n+1}_0 + p^{n+1}_{i-1,j} n_{\mathbb{I}_1} \mathbb{I}^{n+1}_1), \tag{9}$$

where $n_{\mathbb{I}_0}$ and $n_{\mathbb{I}_1}$ indicate the x-component of the normal vector to the fluid–body interface segments $\mathbb{I}^{n+1}_0$ and $\mathbb{I}^{n+1}_1$, respectively, calculated at the time $t = t^{n+1}$. Finally, the volumetric force is approximated by

$$\int_{\mathbb{V}} \left(\frac{1}{\mathrm{Fr}^2} - a_1\right) V \approx \left(\frac{1}{\mathrm{Fr}^2} - a_1\right) \mathbb{V}_{u_{i,j}}. \tag{10}$$

3.4. Fluid interface reconstruction and advection

In the present two-fluid flow model, the free surface is discretized with the volume-of-fluid method due to Hirt and Nichols [6]. To capture the free surface, the known fluid interface geometry is used to compute fluid volume fraction, F, in each pressure cell, $p_{i,j}$ to distinguish between the fluids in the regions Ω_1 and Ω_2. The free surface is defined in the computational cells where a rapid change in density, ρ, and viscosity, ν, occurs. As mentioned earlier, the ratio of the density of the fluid in Ω_1, ρ_1, and the density of the fluid in Ω_2, ρ_2, is set to $\rho_1/\rho_2 = 1/100$ (i.e., $\nu_1/\nu_2 = 1$). The Reynolds numbers for the fluids in Ω_1 and Ω_2 are the same. Thus, only the density in the vicinity of the free surface interface is computed based on the average of the densities ρ_1 and ρ_2 at time $t = t^{n+1}$.

At any time in the solution, the interface is reconstructed using the piecewise linear interface algorithm to approximate free surface and fluid–body interfaces following the works in [7,8]. In this method for every pressure cell $p_{i,j}$ with $0 < F_{i,j} < 1$ one defines an orientation and then a distance of a straight-line segment

$$\vec{n}\vec{x} + d = 0, \tag{11}$$

where F is volume of fluid, unit normal $\vec{n}$ pointed out of fluid and d is a line distance from the origin, which cuts $F_{i,j}$ amount of fluid in cell (see [7,21]). Following the work in [7], an approximation of the fluid interface normal

$$\vec{n} = \frac{\nabla F}{|\nabla F|} \tag{12}$$

is obtained by standard finite difference discretization in every $p_{i,j}$ cell with respect to its neighbours in 3×3 block of cells. It is noted that the fluid–body interface normal is determined based on the geometry of the body. Since the free surface interface is free to move, its advection in time should be performed after the new velocity field has been calculated from the governing equations. In the present numerical algorithm, following the work of Mironova [5], geometrical area-preserving volume-of-fluid advection algorithm of Aulisa et al. [9] is used to advect the free surface in time. The advection algorithm preserves mass exactly for two-dimensional incompressible flows.

The numerical method has been implemented in a computer program developed by Dr. Kocabiyik's research group at Memorial University (see [5] for implementation details). Discrete pressure and velocity fields corresponding to the successive time instants are obtained as a result of solution of a coupled sparse linear system in primitive variables using a generalized minimal residual method. This is done by making use of the Trilinos numerical solver library [13]. At each time iteration, a preconditioned linear system $\mathrm{P}Ax = \mathrm{P}b$ is solved using the generalized minimal residual method, where P is an incomplete LU preconditioner with a threshold. The threshold parameter is chosen so as to minimize the amount of memory needed to store the preconditioner and at the same time to maximize the rate of convergence of the iterative solver. The convergence criteria is $\|\mathrm{P}Ax - \mathrm{P}b\| \leqslant 10^{-6}$.

4. Validation

The numerical algorithm is first tested to determine the accuracy of the spatial and temporal discretizations. The problem of an initial flow past a stationary cylinder in the absence of a free surface at $R = 10^3$ is chosen for the accuracy tests. This Reynolds number is high enough to present the flow structure in detail, yet still low enough to allow for full resolution on fine grids. The relative errors in the predicted quantities are computed at $t = 0.1$ using the discrete L^2 norm defined as

$$\|\bar{\xi} - \xi\| = \Delta h \left(\sum_{i,j} (\bar{\xi}_{i,j} - \xi_{i,j})^2\right)^{1/2}, \tag{13}$$

where $\bar{\xi}$ is the solution obtained by the finest grid possible, ξ is the computed quantity and Δh is the uniform spatial grid step. Since exact analytical solution to this problem is not available, the fully converged numerical predictions obtained with

Table 1
L^2 norm of the relative errors of the pressure, p, and velocity components, u, v, as the time step and the number of grid cells per cylinder diameter vary for the stationary cylinder case in the absence of a free surface at $R = 10^3$ when $t = 0.1$.

	Grid cells per cylinder diameter			Δt		
	40	60	90	0.004	0.002	0.001
$\|\bar{p} - p\|$	0.002677	0.001188	0.000538	0.000491	0.000243	0.000122
$\|\bar{u} - u\|$	0.021027	0.011165	0.005635	0.000575	0.000291	0.000147
$\|\bar{v} - v\|$	0.017875	0.008519	0.003980	0.000597	0.000295	0.000147

the grid system of 120 cells per cylinder diameter are used for full resolution. Three uniform grid systems 90×90, 60×60 and 40×40 are used for the spatial and temporal accuracy tests. The uniform spatial grid step values are $\Delta h = 1/90,\ 1/60,\ 1/40$, respectively. Table 1 shows the calculated spatial and temporal relative errors of the pressure, p, and velocity components, u, v, at $t = 0.1$ as the near wake grid resolution and the time step vary. The results indicate that the present numerical algorithm has an accuracy of second-order in space and of first-order in time, as expected. The computational domain geometry is defined with respect to the *mean* position of the cylinder. In the vicinity of the mean cylinder position, the grid has fine resolution and is uniform. Outside of the uniform grid region, the grid expands exponentially towards the four boundaries of the computational domain. The computational grid geometry is defined by specifying the locations of inflow and outflow boundaries, L_1 and L_2, along the x-axis and the location of the top and bottom boundaries, L_3, along the y-axis as shown in Fig. 5. Numerical experiments indicate that the grid with $L_1 = 20, L_2 = 30, L_3 = 40$ yields results which are accurate to maximum 3% when compared to the reference grid with computational domain size $30 \times 40 \times 60$ for the case of uniform flow past a stationary cylinder in the presence of a free surface at $R = 200$: $\mathrm{Fr} = 0.3, h = 0.55$. This level of accuracy is assumed to be sufficient. The grid resolution tests are carried out for the uniform flow past a stationary cylinder in the presence of a free surface at $R = 200$: $\mathrm{Fr} = 0.3, h = 0.7$. The grids with the grid resolution of 60 cells per diameter give the maximum error of order 2.2% when compared to those with the grid resolution of 90 cells per diameter. Thus, the grid resolution of 60 cells per diameter is chosen for the current investigation of uniform flow past the cylinder in the presence of a free surface. This mesh has approximately 250×190 node points with considerable mesh concentration both around the cylinder 100×100 and in the wake, 150×90, (see Fig. 5). For a Reynolds number of 200, this mesh give a natural shedding frequency of $f_0 = 0.198$. This is within 0.1% of the accepted value of 0.197–0.199 [22,23]. The discussion of spatial grid resolution is in principle the same as that given in [5], and the time step $\Delta t = 0.005$ used for the evolution of the solution follows exactly those set out in that discussion. The accuracy of the numerical algorithm is checked by carrying out computations for the case of uniform flow past a stationary cylinder in the presence of a free surface at $R = 180$. The predicted flow properties are compared to those obtained in the numerical study in [4]. In the work of Reichl et al. [4], the flow is calculated using the computational fluid dynamics commercial software package FLUENT. This package is based on the finite volume method, and uses volume-of-fluid method to treat two flow phase models via a segregated solver on an unstructured boundary fitted grid with a prescribed pressure at the outflow

$$\frac{\partial p}{\partial x} = 0, \qquad \frac{\partial p}{\partial y} = \frac{1}{\mathrm{Fr}^2} \tag{14}$$

and thus, differs from the outflow boundary condition (4) used in the present study. The spatial discretization is performed by a quadratic upstream interpolation for convective kinematics method of Leonard [24]. The temporal discretization is only first-order accurate due to the employment of the volume-of-fluid method. Further details concerning implementation of this software package can be found in the FLUENT manuals. The comparison of the near wake structures between the present computational method and the numerical results of Reichl et al. [4] and Gubanov [14] at $R = 180$, $\mathrm{Fr} = 0.3$ are displayed in Fig. 6 for the cylinder submergence depth, $h = 0.55$. The results are in good agreement. Two-phase flow models with different outflow boundary conditions are used in the present study and the work by Reichl et al. and thus, the free surface is modelled implicitly. A single-fluid flow model is used in [14], and free surface boundary conditions are satisfied explicitly to track the free surface. These differences lead to the minor discrepancies between the numerical results displayed in Fig. 6.

In Table 2, the effect of the submergence depth, h, on predicted values of the local Froude number, $\mathrm{Fr}|_L$, the frequency ratio, $\bar{f}_0/f_0$, ($\bar{f}_0, f_0$: the vortex shedding frequencies in the presence and absence of a free surface, respectively, and $f_0 = 0.191$), the average u-velocity, $\widehat{u}$, at $R = 180$: $\mathrm{Fr} = 0.3$, $h = 0.1, 0.4, 0.55$ are compared with the numerical results of Reichl et al. [4]. The u-velocity is averaged based on the free surface height, $h|_L$, in the region directly above the cylinder. This is undertaken for each Froude number, Fr, and the submergence depth, h, case at the time when maximum lift occurs. For the cases, when no vortex periodic shedding is observed, the average u-velocity is computed close to the point where maximum lift occurs. The local Froude number, $\mathrm{Fr}|_L$, is calculated based on the maximum u-velocity in the region directly above the cylinder, $\bar{u}$, at the time when the lift coefficient reaches its maximum and the free surface height, $h|_L$, by using $\mathrm{Fr}|_L = \bar{u}/\sqrt{(gh|_L)}$. The predicted results are in excellent agreement with the numerical results of Reichl et al. [4].

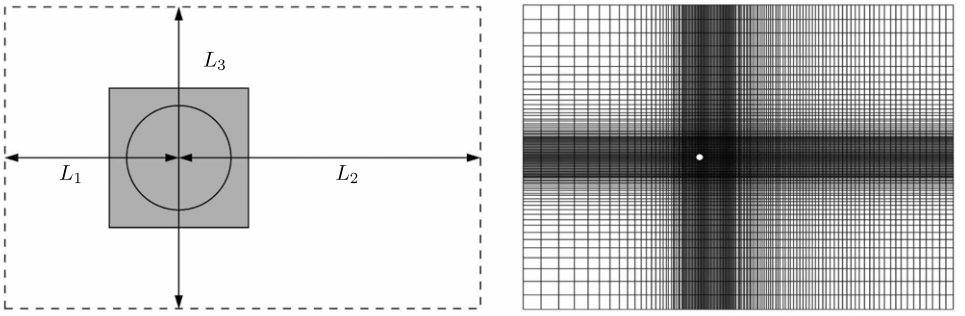

Fig. 5. Grid geometry parameters (left). The shaded region is uniform grid region. Grid used for the majority of the simulations (right). It contains 250×190 cells.

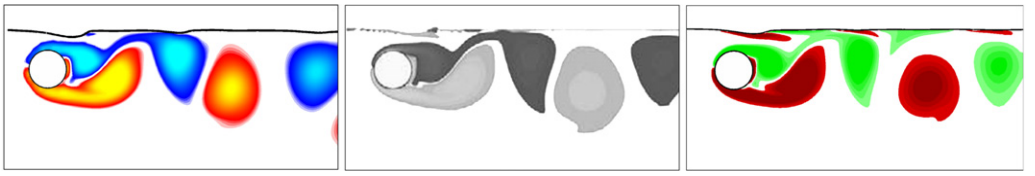

Fig. 6. The equivorticity patterns for the case of uniform flow past a stationary cylinder in the presence of a free surface at $R = 180$, Fr $= 0.3$ and $h = 0.55$: numerical results of Gubanov [14] (left); Reichl et al. [4] (middle) and present results (right).

Table 2
The effect of the submergence depth, h, on the local Froude number, $\mathrm{Fr}|_L$; the frequency ratio, $\bar{f}_0/f_0$; the average u-velocity in the region directly above the cylinder, $\widehat{u}$, for uniform flow past a stationary cylinder in the presence of a free surface at $R = 180$: Fr $= 0.3$, $h = 0.1, 0.4, 0.55$. Comparison with the numerical results of Reichl et al. [4].

	Reichl et al. [4]			Present		
h	$\mathrm{Fr}\|_L$	$\bar{f}_0/f_0$	$\widehat{u}$	$\mathrm{Fr}\|_L$	$\bar{f}_0/f_0$	$\widehat{u}$
0.10	1.09	–	0.70	1.09	–	0.71
0.40	0.73	1.01	1.35	0.73	1.00	1.34
0.55	0.66	1.07	1.41	0.66	1.07	1.41

5. Results

The numerical simulations for two-dimensional flow past a circular cylinder subject to forced in-line oscillations beneath a free surface are carried out at the Reynolds number of $R = 200$: $A = 0.13$, Fr $= 0.2$, $h = 0.25, 0.5, 0.75$ when $f/f_0 = 1.5, 2.5, 3.5$. The unsteady flow calculations are conducted for the time up to $t = 100$ when $h = 0.25, 0.5, 0.75$ and up to $t = 150$ in the absence of free surface ($h = \infty$) based on the grid system $20 \times 30 \times 40$ with 252×196 elements and the time step, $\Delta t = 0.005$. The predicted natural vortex shedding frequency at $R = 200$ is $f_0 = 0.198$. The numerical results are visualized in terms of equivorticity and pressure contours in the near wake region. All the snapshots that follow, $t = 0T$ corresponds to the instant when the cylinder reaches its maximum displacement, $x(t) = A$. In all the equivorticity and the pressure contour plots that follow, black colours correspond to counter-clockwise rotation (positive) and gray colours indicate clockwise rotation (negative). For streamwise oscillations of the cylinder, the range near $f/f_0 \approx 2$ constitutes the fundamental lock-on regime (the unsteady pressures from the wake vortices induce the cylinder to respond). Certain wake patterns can be induced by the forced body motion, such as the **2S** mode (two single vortices per cycle, like the classic Kármán street), **2P** mode (two vortex pairs per cycle), and **P** + **S** (one single and a pair of vortices per cycle), following the terminology introduced in [25]. The determination of locked-on regimes of vortex shedding is based on the repetition of vortex shedding in the near wake region over an integer number of cylinder oscillation periods following the work of Ongoren and Rockwell [26]. Thus, a single vortex shedding cycle, T_v, is defined by $T_v = nT$, where n is an integer number. The coalescence of vortices may result in **C**(**2S**) (or **C**(**P** + **S**) or **C**(**2S** + **2P**)) mode. For example, in **C**(**2S**) mode at least one shed vortex is formed by the smaller vortices coalesce.

5.1. Cylinder submergence depth, $h = 0.5$

Table 3 summarizes the effect of the free surface inclusion at $h = 0.5$ on the flow regimes, the vortex shedding modes and their periods, T_v, for the case Fr $= 0.2$ when $f/f_0 = 1.5, 2.5, 3.5$, respectively. For $f/f_0 = 1.5$, a transition occurs from quasi-periodic state (**C**(**6S**) mode, per $5T$, within $T \le t \le 14T$) to non-periodic state ($14T \le t \le 23T$); and then to quasi-periodic state (**4S** mode, per $3T$, within $23T \le t \le 29T$). The presence of the free surface seems to destabilize the flow with

Table 3
The effect of the free surface inclusion on vortex shedding modes and their periods, T_v, for the case Fr $= 0.2$ and $h = 0.5$ at $R = 200$: $A = 0.13$, $f/f_0 =$ 1.5, 2.5, 3.5. The superscript "*" denotes quasi-locked-on modes.

f/f_0	$h = 0.5$		$h = \infty$	
	Mode	T_v	Mode	T_v
1.5	**C**(**6S**)* ($T \le t \le 14T$); Non-locked ($14T < t < 23T$); **4S*** ($23T \le t \le 29T$)	$5T$ – $3T$	**2P**	$2T$
2.5	Non-locked	–	**C**(**6S**)*	$8T$
3.5	**C**(**2S**)* ($21T \le t \le 33T$); Non-locked ($34T \le t \le 69T$)	$4T$	**C**(**2S**)* ($50T \le t \le 71T$); Non-locked ($72T \le t \le 104T$)	$4T$

an increase in the frequency ratio from $f/f_0 = 1.5$ to $f/f_0 = 2.5$. For the highest frequency ratio, $f/f_0 = 3.5$, the classical quasi-locked-on **C**(**2S**) mode, per $4T$, is observed within twelve periods of cylinder oscillation, and then, a transition into the non-periodic state occurs ($34T \le t \le 69T$). The details of the new quasi-locked-on vortex shedding modes, **C**(**6S**), are given only for the frequency ratio, $f/f_0 = 1.5$.

In Fig. 7, the equivorticity patterns and the pressure contours over five periods of cylinder motion, $5T$, are displayed when $f/f_0 = 1.5$, ($T \le t \le 14T$). The quasi-locked-on **C**(**6S**) mode, per $5T$, is observed. This mode is a combination of three classical **2S** modes. Two co-rotating positive vortices "3" and "4" merge to produce the large single vortex, "4 + 3", over $T/2 < t < T$, and the cylinder alternately sheds two single vortices from lower and upper sides, respectively, over $0T \le t \le 3T/2$ ("4 + 3" is shed at $t \approx T$; "1" is shed at $t \approx 3T/2$). Then, the positive vortex, "6", developing $T/2 \le t \le 2T$ becomes detached at $t \approx 2T$. On the other hand, the negative vortex, "2", developed over $T \le t \le 3T$ is shed at $t \approx 7T/2$. Over the last two periods of vortex shedding cycle ($3T \le t \le 5T$), two more single vortices, "10 + 8" and "5", are alternately shed from lower and upper sides of the cylinder at $t \approx 4T$ and $t \approx 9T/2$, respectively. Thus, the cylinder alternately sheds three single positive vortices and three single negative vortices from lower and upper sides, respectively, over $0T \le t \le 5T$. Therefore, the quasi-locked-on **C**(**6S**) mode, per $5T$, is observed for $f/f_0 = 1.5$ when $h = 0.5$ within $T \le t \le 14T$. The corresponding pressure plots displayed in Fig. 7 reveal that the high pressure region develops in the stagnation region; and above and below the low pressure region in the downstream of the cylinder at $t = 0T$. Moreover, at $t = 0T$ the low pressure region concentration is observed rear of the cylinder. By the development of the positive vortex, "6", over $0T \le t \le T/2$ the high pressure from the stagnation region starts moving in the clockwise direction, whereas the lowest pressure region is shifted substantially to the lower side of the cylinder. Then, the high pressure region from the stagnation region moves in the counter-clockwise direction over $T \le t \le 2T$, in which two negative vortices, "2" and "5", develop. On the other hand, the low pressure region is substantially formed in the rear of the cylinder at $t \approx 2T$ when the positive vortex, "6", becomes detached. Over $5T/2 \le t \le 9T/2$, the high pressure region associated with the stagnation region starts to move in the clockwise direction and it extends above and below the low pressure region at $t \approx 9T/2$ by the shedding of the negative vortex, "5". At the same time, the low pressure region is concentrated rear and upper right side of the cylinder.

5.2. Cylinder submergence depth, $h = 0.75$

The effect of the free surface inclusion at $h = 0.75$ on the flow regimes, the vortex shedding modes and their periods, T_v, is summarized in Table 4, respectively. The presence of the free surface seems to break up the periodicity of the vortex shedding when $f/f_0 = 1.5$. The period of vortex shedding mode is $2T$ for $f/f_0 = 1.5$ in the absence of free surface. The coalescence between the vortices in the vortex shedding layers appears at the higher frequency ratios, $f/f_0 = 2.5$ and 3.5, for both $h = 0.75$ and $h = \infty$. For $f/f_0 = 2.5$ and 3.5, a switchover in the vortex shedding modes is observed as h decreases from ∞ to $h = 0.75$. It is also noted that in the absence of free surface a switchover from **2P** to quasi-locked-on **C**(**6S**) and **C**(**2S**) modes is observed with an increase in the value of the frequency ratio, f/f_0. On the other hand, as the frequency ratio, f/f_0, increases, the presence of free surface at $h = 0.75$ seems to stabilize the vortex shedding mode to the quasi-locked-on **C**(**P** + **S**) + **C**(**2S**) mode for both $f/f_0 = 2.5$ and 3.5. The details of this new vortex shedding mode will be given only for the frequency ratio, $f/f_0 = 3.5$.

The equivorticity patterns and the pressure contours are displayed in Fig. 8 in the near wake of the cylinder over seven periods of cylinder oscillation, $7T$, when $f/f_0 = 3.5$. The vortex shedding mode is the quasi-locked-on **C**(**P** + **S**) + **C**(**2S**) mode, per $7T$, within twenty-six periods of cylinder oscillation, $26T$, ($4T \le t \le 30T$). A transition into the non-periodic state is observed when the switching time is reached at $t \approx 30T$, and then flow shows non-periodic behaviour within $31T \le t \le 69T$. The **C**(**P** + **S**) + **C**(**2S**) mode is the combination of the two classical **C**(**P** + **S**) and **C**(**2S**) modes. Fig. 8 shows that the cylinder alternately sheds a single vortex from each sides, namely the vortex "3" from lower side ($t \approx T$) and the vortex "2 + 1" from upper side ($t \approx 5T/2$). Then, it sheds the single vortex "10 + 8 + 6 + 4" ($t \approx 5T$) and the pair of co-rotating vortices "11" and "9 + 7 + 5" ($t \approx 6T$) from positive and negative vortex shedding layers, respectively. It is noted that the development of each vortex is a result of coalescence of smaller co-rotating vortices in the vortex shedding layer.

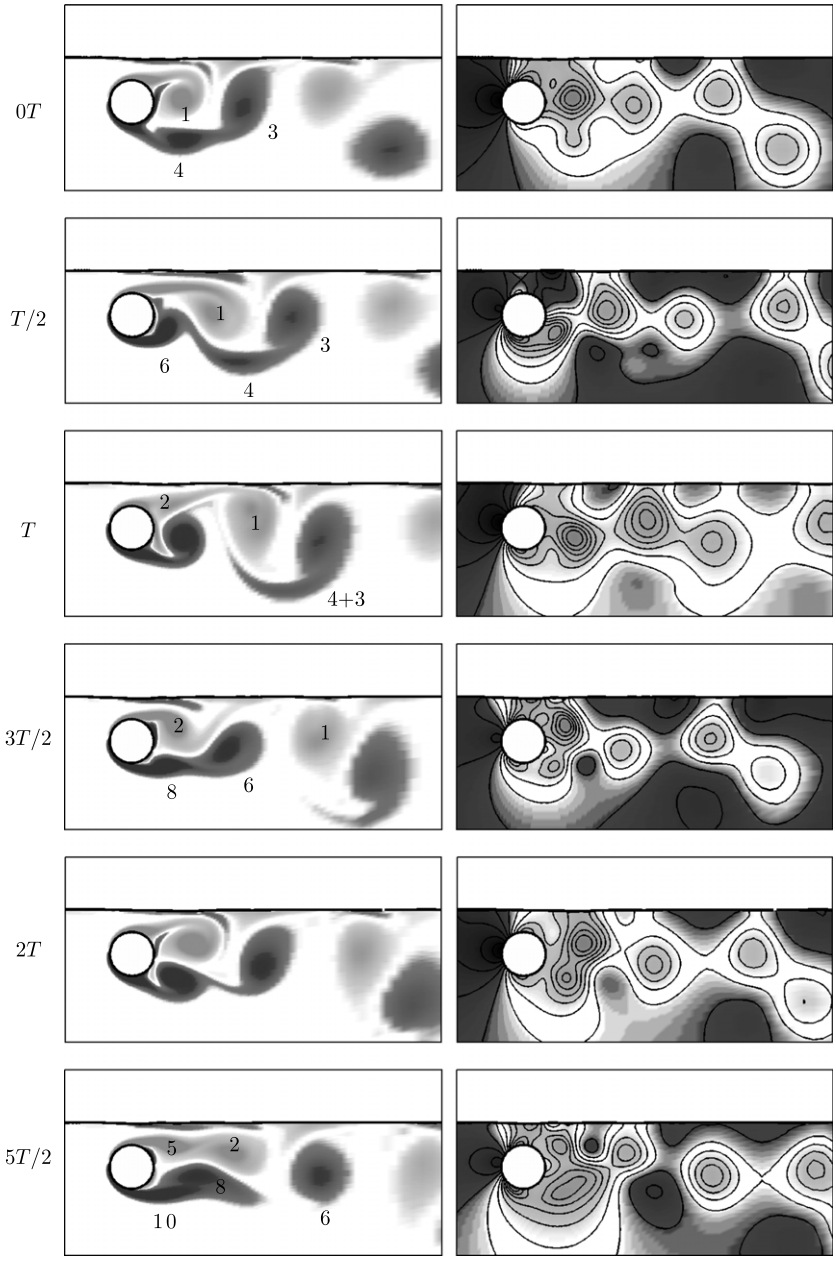

Fig. 7. The equivorticity patterns (left) and the pressure contours (right) in the near wake over $5T$, at $R = 200$: $A = 0.13$, $f/f_0 = 1.5$ when Fr $= 0.2$ and $h = 0.5$ [$T \approx 3.367$, $23.569 \leq t \leq 40.404$: ($7T$, $12T$) or symbolically ($0T$, $5T$)]. The quasi-locked-on **C**(**6S**) mode, per $5T$, is observed ($t \leq 14T$).

Thus, this vortex shedding mode is designated as the quasi-locked-on $\mathbf{C}(\mathbf{P}+\mathbf{S})+\mathbf{C}(\mathbf{2S})$ mode, per $7T$. An examination of the pressure plots indicates that the positive vortices represent the regions of the lowest pressure and thus the near wake is controlled by the positive vortex structures. Moreover, the pronounced variations in the free surface level enhance the high and low pressure regions near the curved free surface interface. The highest pressure region associated with the stagnation switches from the stagnation region and the region directly above the cylinder to the region in the upper left side of the cylinder where the free surface rises sufficiently in this region, at ($t = nT/2$, $n = 1, 3, 5, 7, 9, 11, 13$). On the other hand, the low pressure region develops rear and upper left side of the cylinder near the free surface interface at $t = 0T$. Then, it shifts to the regions below and directly above the cylinder when the free surface falls in this region, at $t = T/2$. This switching process in the location of the low pressure region is observed at every half period of cylinder oscillation, $T/2$, ($t = nT/2$, $n = 1, 3, 5, 7, 9, 11, 13$).

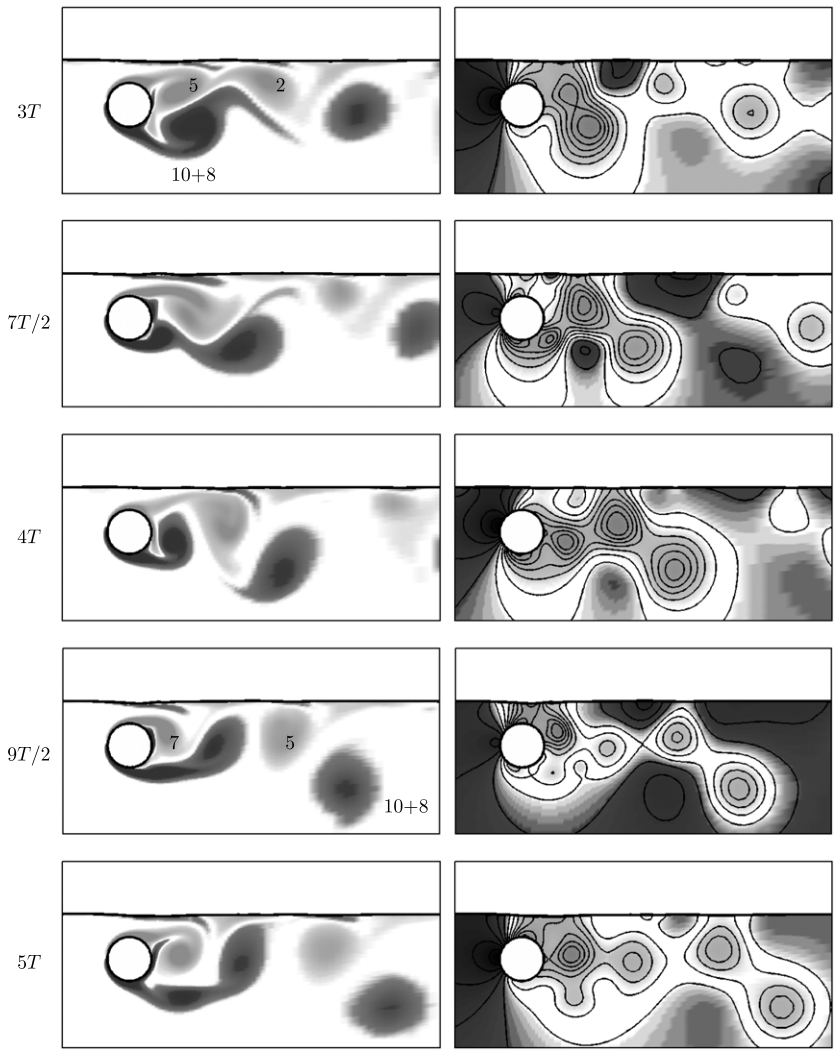

Fig. 7. (*continued*)

Table 4
The effect of the free surface inclusion on vortex shedding modes and their periods, T_v, for the case Fr $= 0.2$ and $h = 0.75$ at $R = 200$: $A = 0.13$, $f/f_0 = 1.5, 2.5, 3.5$. The superscript "*" denotes quasi-locked-on modes.

f/f_0	$h = 0.75$		$h = \infty$	
	Mode	T_v	Mode	T_v
1.5	Non-locked	–	**2P**	$2T$
2.5	$[\mathbf{C}(\mathbf{P}+\mathbf{S})+\mathbf{C}(\mathbf{2S})]^*$ ($3T \le t \le 40T$); Non-locked ($41T \le t \le 49T$)	$5T$	$\mathbf{C}(\mathbf{6S})^*$	$8T$
3.5	$[\mathbf{C}(\mathbf{P}+\mathbf{S})+\mathbf{C}(\mathbf{2S})]^*$ ($4T \le t \le 30T$); Non-locked ($31T \le t \le 69T$)	$7T$	$\mathbf{C}(\mathbf{2S})^*$ ($50T \le t \le 71T$); Non-locked ($72T \le t \le 104T$)	$4T$

6. Summary and conclusions

The problem of unsteady, laminar, two-dimensional flow of a viscous incompressible fluid past a circular cylinder subject to in-line oscillations in uniform flow in the presence of the free surface is investigated numerically. The method of solution is based on a finite volume discretization of the two-dimensional unsteady continuity and Navier–Stokes equations (when a

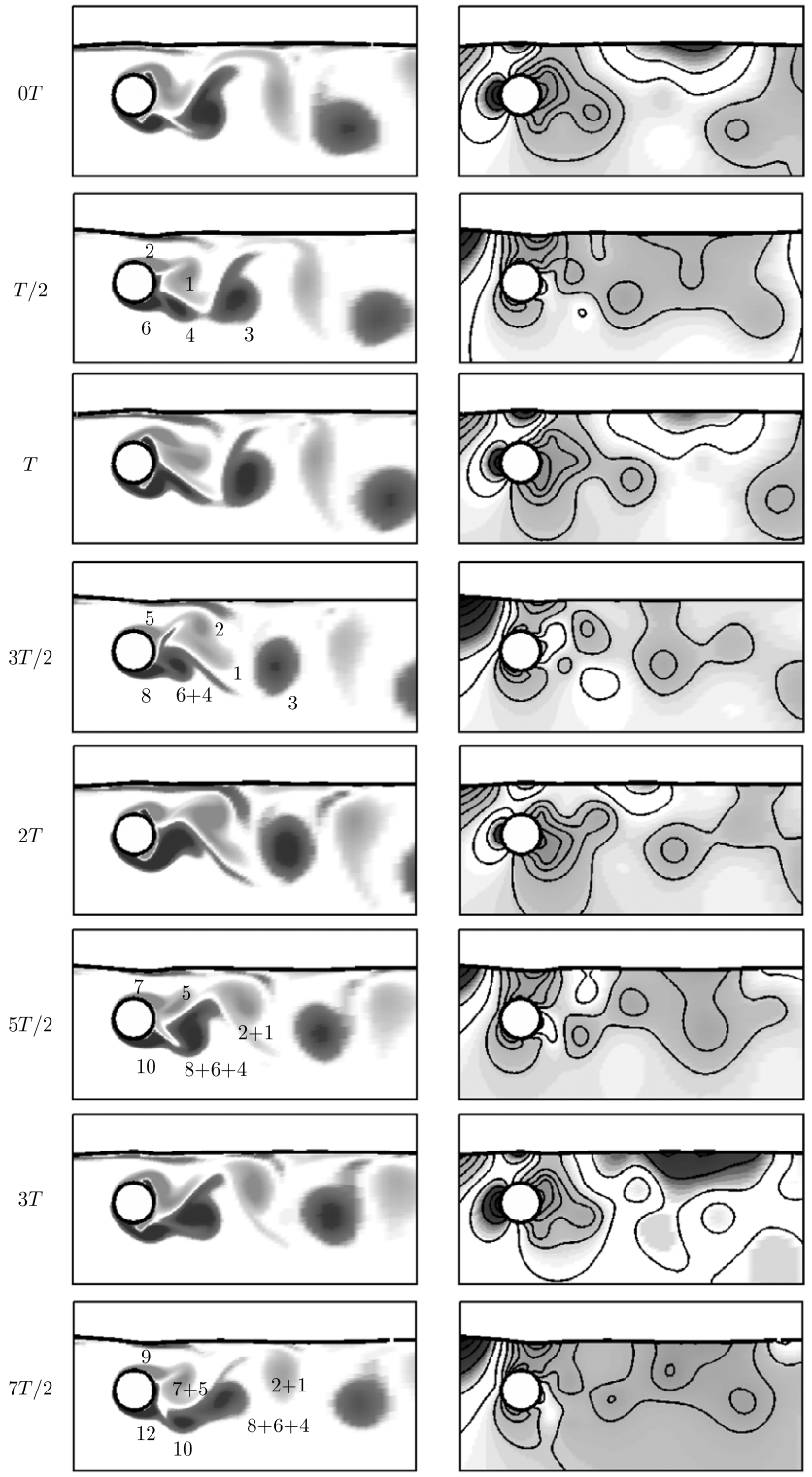

Fig. 8. The equivorticity patterns and the pressure contours in the near wake over seven periods of cylinder oscillation, $7T$, at $R = 200$: $A = 0.13$, $f/f_0 = 3.5$ when Fr $= 0.2$ and $h = 0.75$ [$T \approx 1.443$, $30.303 \leq t \leq 40.404$: $(21T, 28T)$ or symbolically $(0T, 7T)$]. The quasi-locked-on $\mathbf{C}(\mathbf{P}+\mathbf{S}) + \mathbf{C}(\mathbf{2S})$ mode, per $7T$, is observed ($4T \leq t \leq 30T$).

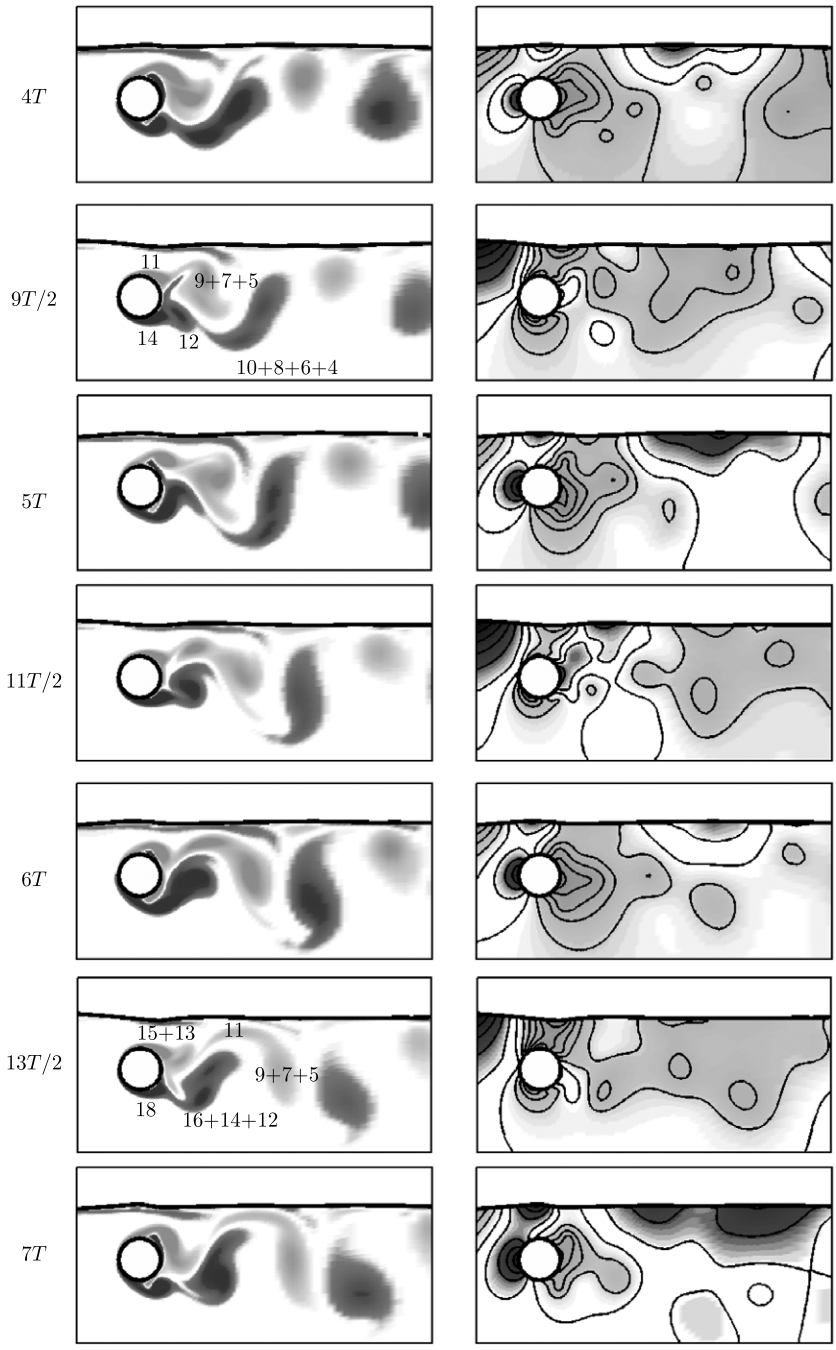

Fig. 8. (*continued*)

solid body present) in their pressure–velocity formulation on a fixed Cartesian grid. The two-fluid model based on volume-of-fluid method is used to discretize the free surface interface. The free surface is defined in the computational cells where a rapid change in density, ρ, and viscosity, μ, occurs: $\rho_{\text{air}}/\rho_{\text{water}} = 1/100$, $\mu_{\text{air}}/\mu_{\text{water}} = 1/100$ (see, for example, [4]). The accuracy checks indicate that the present method is of second-order in space and first-order in time. The code validations in special cases show good comparisons with previous numerical results.

The fluid flow is calculated at the Reynolds number of $R = 200$ and the displacement amplitude $A = 0.13$ for the frequency ratios $f/f_0 = 1.5, 2.5, 3.5$ when $\text{Fr} = 0.2$ and $h = 0.25, 0.5, 0.75$. The effects of the cylinder submergence depth, h, and the frequency ratio, f/f_0, on the equivorticity patterns in the near wake region are summarized in Fig. 9.

Table 5
The effects of the free surface inclusion, the cylinder submergence depth, h (=0.25, 0.5, 0.75) and the frequency ratio, f/f_0 (=1.5, 2.5, 3.5), on vortex shedding modes and their periods, T_v, at $R = 200$: $A = 0.13$, Fr $= 0.2$. The superscript "*" denotes quasi-locked-on modes.

f/f_0	$h = 0.25$		$h = 0.5$		$h = 0.75$		$h = \infty$	
	Mode	T_v	Mode	T_v	Mode	T_v	Mode	T_v
1.5	**C**(**2S**)* ($11T \le t \le 29T$)	$2T$	**C**(**6S**)* ($T \le t \le 14T$); Non-locked ($14T < t < 23T$); **4S*** ($23T \le t \le 29T$)	$5T$ – $3T$	Non-locked	–	**2P**	$2T$
2.5	**C**(**2S**)* ($7T \le t \le 31T$) Non-locked ($32T \le t \le 49T$)	$4T$	Non-locked	–	[**C**(**P** + **S**) + **C**(**2S**)]* ($3T \le t \le 40T$) Non-locked ($41T \le t \le 49T$)	$5T$	**C**(**6S**)*	$8T$
3.5	**C**(**2S**)* ($21T \le t \le 32T$) Non-locked ($32T < t < 34T$) **C**(**2S**)* ($34T \le t \le 43T$) Non-locked ($44T \le t \le 43T$)	$4T$	**C**(**2S**)* ($21T \le t \le 33T$) Non-locked ($34T \le t \le 69T$)	$4T$	[**C**(**P** + **S**) + **C**(**2S**)]* ($4T \le t \le 30T$) Non-locked ($31T \le t \le 43T$)	$7T$	**C**(**2S**)* ($50T \le t \le 71T$) Non-locked ($72T \le t \le 104T$)	$4T$

The case when the free surface is absent ($h = \infty$) is also shown in this figure. The snapshots are taken at the instant $x(t) = A$. It is noted that for the periodic/quasi-periodic cases the snapshots are taken over the time interval in which the flow reaches a periodic/quasi-periodic state. For non-periodic cases, the commonly appearing equivorticity plots at $x(t) = A$ (within the time interval $25T \le t \le 100$) are also shown in the figure. It is seen that minimal free surface deformations occur at $h = 0.75$, and for all f/f_0. Thus, there is a diffusion of the opposite signed vorticity across the interface. As the cylinder submergence depth, h, decreases to 0.25, the interface curvature becomes more pronounced (only slightly) for each frequency ratio, f/f_0. At the smallest frequency ratio, $f/f_0 = 1.5$, the lower vortex shedding layer shows a similar behaviour irrespective of the presence of a free surface. On the other hand, inclusion of the free surface seems to cause a change in the vortex formation from the upper side of the cylinder: the shed negative vortex is lifted upward toward the free surface interface for each $h = 0.25, 0.5, 0.75$; and attaches to the free surface at $h = 0.25, 0.5$ at the same frequency ratio, $f/f_0 = 1.5$. For the higher frequency ratios, $f/f_0 = 2.5, 3.5$, the near wake shows a quite similar behaviour in the presence of free surface at $h = 0.5, 0.75$, when compared to that at $h = \infty$. At the smallest cylinder submergence depth, $h = 0.25$, the near wake is dissimilar to the cases at $h = 0.5, 0.75$, especially for $f/f_0 = 2.5$. When $h = 0.25$ the negative vorticity diffuses across the interface due to the interaction with the free surface for all f/f_0. At larger cylinder submergence depths, $h = 0.5, 0.75$, the shed negative vortex is lifted upward toward the free surface by the propagation of the positive vortices as f/f_0 increases. This results in the elongation of the negative vortices in the horizontal direction, and they become weaker as they reach the free surface. Thus, the near wake becomes more dominated by positive vortex structures and it seems to be more skew symmetric as the cylinder submergence depth, h, decreases from ∞ to 0.25. It is also seen that, the vortex formation length (length of the positive vortex developing in the lower vortex shedding layer) remains almost the same as h decreases from ∞ to 0.5 for the frequency ratios, $f/f_0 = 1.5, 2.5$. On the other hand, an increase in the frequency ratio, f/f_0, from 2.5 to 3.5 results in an increase (or a decrease) in the vortex formation length by approximately 21.5%, 26.3% and 34.4% (or 9.3%) for the cylinder submergence depths, $h = 0.5$, $h = 0.75$ and $h = \infty$ (or $h = 0.25$), respectively. Moreover, the amount of the opposite signed vorticity near the free surface interface increases as the frequency ratio, f/f_0, increases from 1.5 to 3.5 in the presence of the free surface at $h = 0.25, 0.5, 0.75$. Minimal free surface deformations become more pronounced with the increased frequency ratio as expected (see [4]).

Table 5 summarizes the effects of free surface inclusion, cylinder submergence depth, h, and the frequency ratio, f/f_0, on the vortex shedding modes and their periods, T_v. This investigation has shown that it is possible to generate distinctly different patterns of vortex formation than that of classical vortex shedding modes [**2S** (or **C**(**2S**)), **2P** (or **C**(**2P**)), **P** + **S** (or **C**(**P** + **S**))] in the presence of the free surface depending on the values of the cylinder submergence depth, h, and the frequency ratio, f/f_0. These new vortex shedding modes are the combination of the two and three **2S** modes; **C**(**P** + **S**) and **C**(**2S**) modes i.e., **4S** and **6S** (or **C**(**6S**)) mode; **C**(**P**+**S**)+**C**(**2S**) mode. At the smallest frequency ratio, $f/f_0 = 1.5$, the presence of the free surface seems to destabilize the flow at $h = 0.75$ when compared to the reference case $h = \infty$. A decrease in the value of h, from 0.75 to 0.5, results in the stabilization of the flow, and the occurrence of new vortex shedding modes (quasi-locked-on **C**(**6S**) mode, per $5T$ and quasi-locked-on **4S** mode, per $3T$) for $f/f_0 = 1.5$. The quasi-locked-on **C**(**2S**) mode, per 2T, is observed at $h = 0.25$ for $f/f_0 = 1.5$. This mode persists for the higher frequency ratios, $f/f_0 = 2.5$ and 3.5 when $h = 0.25$. As the frequency ratio, f/f_0, increases from 1.5 to 2.5, the vortex shedding is stabilized and produces different modes of vortex shedding, **C**(**P** + **S**) + **C**(**2S**), per $5T$, at $h = 0.75$. On the other hand, the flow shows non-periodic behaviour for the smaller cylinder submergence depth, $h = 0.5$, when $f/f_0 = 2.5$. An interesting point to note is that for the

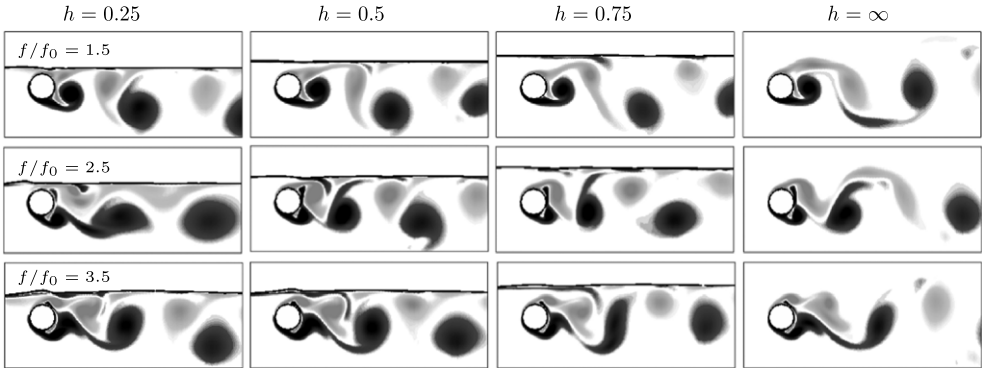

Fig. 9. The effects of the cylinder submergence depth, h, and the frequency ratio, f/f_0, on the equivorticity patterns at $R = 200$: $A = 0.13$, Fr $= 0.2$.

smaller frequency ratios, $f/f_0 = 1.5$ and 2.5, the presence of the free surface at each cylinder submergence depth causes a switchover in the vortex shedding modes when compared to the reference case $h = \infty$. On the other hand, at the highest frequency ratio, $f/f_0 = 3.5$, the quasi-locked-on **C**(**2S**) mode, per $4T$, persists irrespective of the presence of a free surface, except the case when $h = 0.75$. The vortex shedding period, T_v, increases from $2T$ to $4T$ and $8T$ when $h = 0.25$ and $h = \infty$, respectively, with an increase in the frequency ratio, f/f_0, from 1.5 to 2.5. However, as f/f_0 increases from 2.5 to 3.5, the vortex shedding period, T_v, remains fixed at $4T$ when $h = 0.25$; increases from $5T$ to $7T$ at $h = 0.75$, and decreases from $8T$ to $4T$ at $h = \infty$.

An examination of the pressure plots at $t = 0T$ (when the cylinder reaches its maximum displacement, $x(t) = A$) indicates that high pressure region is associated with the front stagnation region for the cases $h = 0.25, 0.5, 0.75, h = \infty$ when $f/f_0 = 1.5$; $h = 0.5, 0.75$ when $f/f_0 = 3.5$; and $h = \infty$ when $f/f_0 = 2.5, 3.5$. However, for the frequency ratio, $f/f_0 = 2.5$, the high pressure concentration substantially occurs at the upper left side of the cylinder at $t = 0T$ when $h = 0.25, 0.5, 0.75$ unlike the reference case $h = \infty$. On the other hand, at $t = 0T$ low pressure mainly concentrates the rear or the bottom and above of the cylinder by the development of the new vortices irrespective of the cylinder submergence depth, h, and the frequency ratio, f/f_0 (see Figs. 7 and 8) (the vorticity and pressure plots are not presented in this paper for the cases $h = \infty$ and $h = 0.25$). In addition, the positive vortices located through the downstream of the cylinder represents the low pressure regions irrespective of the presence of the free surface for all f/f_0. The pronounced variations in the free surface level, in general, enhance the high and low pressure regions near the curved free surface interface. That is, the highest pressure region associated with the stagnation switches from the stagnation region to the region in the upper left side of the cylinder where the free surface rises sufficiently in this region (or vice versa) for the cases $h = 0.25, 0.5, 0.75$ when $f/f_0 = 3.5$ (or for the case $h = 0.25$ when $f/f_0 = 2.5$) at every half cycle of the cylinder oscillation, $T/2$. On the other hand, the low pressure becomes dominated in the downstream of the cylinder when a positive vortex is shed into the lower vortex shedding layer irrespective of the presence of the free surface and for all frequency ratios, f/f_0.

Acknowledgement

The financial support for this research is provided by the Natural Sciences and Engineering Research Council of Canada. Computer program for this research is developed while the fourth author was at Memorial University.

References

[1] J. Carberry, Wake states of a submerged oscillating cylinder and of a cylinder beneath a free surface, Ph.D. Thesis, Monash University, 2002.
[2] O. Cetiner, D. Rockwell, Streamwise oscillations of a cylinder in steady current. Part 2. Free-surface effects on vortex formation and loading, Journal of Fluid Mechanics 427 (2001) 29–59.
[3] J. Sheridan, J.-C. Lin, D. Rockwell, Flow past a cylinder close to a free surface, Journal of Fluid Mechanics 330 (1997) 1–30.
[4] P. Reichl, K. Hourigan, M.C. Thompson, Flow past a cylinder close to a free surface, Journal of Fluid Mechanics 533 (2005) 269–296.
[5] L. Mironova, Accurate computation of free surface flow with an oscillating circular cylinder based on a viscous incompressible two-fluid model, Ph.D. Thesis, Memorial University of Newfoundland, 2008.
[6] C.W. Hirt, B.D. Nichols, Volume of fluid (VOF) method for the dynamics of free boundaries, Journal of Computational Physics 39 (1981) 201–225.
[7] J. Gerrits, Dynamics of liquid-filled spacecraft, Ph.D. Thesis, University of Groningen, 2001.
[8] W.J. Rider, D.B. Kothe, Reconstructing volume tracking, Journal of Computational Physics 141 (2) (1998) 112–152.
[9] E. Aulisa, S. Manservisi, R. Scardovelli, S. Zaleski, A geometrical area-preserving volume-of-fluid advection method, Journal of Computational Physics 192 (1) (2003) 355–364.
[10] R. Scardovelli, S. Zaleski, Interface reconstruction with least-square fit and split Eulerian–Lagrangian advection, International Journal for Numerical Methods in Fluids 41 (3) (2003) 251–274.
[11] D.J.E. Harvie, D.F. Fletcher, A new volume of fluid advection algorithm: the stream scheme, Journal of Computational Physics 162 (1) (2000) 1–32.
[12] C.W. Hirt, J.M. Sicilian, A Porosity Technique for the definition of Obstacles in Rectangular Cell Meshes, Flow Science, Inc., Los Alamos, New Mexico, 1985.
[13] M. Sala, M.A. Heroux, D.M. Day, Trilinos tutorial, Sandia Report No. SAND2004-2189, Sandia National Laboratories, Albuquerque, New Mexico.

[14] O. Gubanov, Design of CFD code using high level programming paradigms: free surface flows with arbitrarily moving rigid bodies, Master's Thesis, Memorial University of Newfoundland, 2006.
[15] F. Farassat, Introduction to generalized functions with applications in aerodynamics and aeroacoustics, NASA Technical Paper No. 3428, Langley Research Center, Hampton, Virginia.
[16] G. Fekken, Numerical simulation of free-surface flow with moving rigid bodies, Ph.D. Thesis, University of Groningen, 2004.
[17] K.M.T. Kleefsman, Water impact loading on offshore structures. A numerical study, Ph.D. Thesis, University of Groningen, 2005.
[18] P.M. Gresho, R.L. Sani, Incompressible Flow and the Finite Element Method, John Wiley and Sons, Inc., New York, 1998.
[19] J. Gerrits, A. Veldman, Numerical simulation of coupled liquid–solid dynamics, in: Onate, E. Bugeda, G. and Suarez, B. (Eds.) Proceedings of the European Congress on Computational Methods in Applied Sciences and Engineering, Barcelona, Spain, 2000.
[20] H.K. Versteeg, W. Malalasekera, An Introduction to Computational Fluid Dynamics. The Finite Volume Method, Longman Scientific and Technical, UK, 1995.
[21] J.E. Pilliod Jr., E.G. Puckett, Second-order accurate volume-of-fluid algorithms for tracking material interfaces, Journal of Computational Physics 199 (2) (2004) 465–502.
[22] P. Poncet, Topological aspects of three-dimensional wakes behind rotary oscillating cylinders, Journal of Fluid Mechanics 517 (2004) 27–53.
[23] R.D. Henderson, Nonlinear dynamics and pattern formation in turbulent wake transition, Journal of Fluid Mechanics 352 (1997) 65–112.
[24] B.P. Leonard, A stable and accurate convective modelling procedure based on quadratic upstream interpolation, Computer Methods in Applied Mechanics and Engineering 19 (1979) 59–98.
[25] C.H.K. Williamson, A. Roshko, Vortex formation in the wake of an oscillating cylinder, Journal of Fluids and Structures 2 (1988) 355–381.
[26] A. Ongoren, D. Rockwell, Flow structure from an oscillating cylinder. Part 2. Mode competition in the near wake, Journal of Fluid Mechanics 191 (1988) 225–245.